Adsorption (2011) 17: 55–68
DOI 10.1007/s10450-010-9289-z

A novel and consistent method (TriPOD) to characterize an arbitrary porous solid for its accessible volume, accessible geometrical surface area and accessible pore size

L.F. Herrera · Chunyan Fan · D.D. Do · D. Nicholson

Received: 9 May 2010 / Accepted: 26 October 2010 / Published online: 6 November 2010

Abstract We present an improved Monte Carlo integration method to calculate the accessible pore size distribution of a porous solid having known configuration of solid atoms. The pore size distribution obtained with the present method is consistent with the accessible volume and the accessible geometric surface area presented in previous publications (Do and Do, in J. Colloid Interface Sci. 316(2):317–330, 2007; Do et al. in Adsorpt. J., 2010). The accessible volume, accessible geometrical surface area and the pore size distribution method construct an unambiguous and robust single framework to characterize porous solids. This framework is based on the derivation of the space accessible to the center of mass of a probe molecule. The accessible pore size presented is an absolute quantity in the sense that a zero value is possible. We present the entire framework of this characterization method and compare the improved method with the one presented previously for a set of porous solids such as graphitic slit pores, defective slit pores, bundle of carbon nanotubes, zeolite and some metal organic frameworks.

Keywords Characterization · Adsorption · Monte Carlo integration · Pore size distribution · Accessibility

1 Introduction

The characterization of porous solids has been an important area of research for many decades (Gregg and Sing 1982; Rouquerol et al. 1994, 1999; Sing et al. 1985; Kaneko et al. 2002). This is because the developments of new technologies and new materials require a more detailed understanding of the structure of porous solids. Most solids do not have well defined geometrical shapes, such as slit, cylinder and spheres, and therefore they are not amenable to the classical methods (Barrett et al. 1951; Broekhoff and De Boer 1968; Dubinin and Stoeckli 1980; Horvath and Kawazoe 1983; Saito and Foley 1991) summarized in Table 1. Some examples of this type of solids are alumina, silica gel and metal organic frameworks (Li et al. 1999; Rowsell and Yaghi 2004). Recently, Do and co-workers (Do et al. 2008a) have presented a new definition of pore size (the so-called *accessible* pore size), this concept is applicable to porous solids whose structure is known. Using this definition, they have derived analytical solutions of *accessible* pore size distribution (PSD) for some model pores whose structures vary from simple to complex configurations (Do et al. 2010). From the analytical solutions obtained from this work (Do et al. 2010) for some ideal pores, we establish that the original method proposed in Do et al. (2008a) fails to locate the largest sphere that can be fitted into the accessible space. Therefore, it is our goal to develop an improved Monte Carlo integration method based on the definition of accessible pore size given in Do et al. (2010).

L.F. Herrera · C. Fan · D.D. Do (✉) · D. Nicholson
School of Chemical Engineering, University of Queensland, St. Lucia, Qld 4072, Australia
e-mail: d.d.do@uq.edu.au

2 Theory

2.1 Accessible pore volume

We define the accessible pore volume (V_{acc}) as the volume accessible to the center of mass of a particle at zero loading (Do and Do 2007). The accessible volume can be calculated for a porous solid whose atomistic configuration is known by using a Monte Carlo integration method as follows. We

Table 1 Some classical theories developed for surface area and pore size distribution

Theory	Year	Solids	Assumptions	
			Pore shape	Reference
Barrett, Joyner and Halenda	1951	Mesoporous	Slit and Cylinder	(Barrett et al. 1951)
Broekhoff-de Boer	1968	Mesporous	Slit and Cylinder	(Broekhoff and De Boer 1968)
Dubinin-Stoeckli	1980	Microporous	Slit	(Dubinin and Stoeckli 1980)
Horvath-Kawazoe	1983	Microporous	Slit	(Horvath and Kawazoe 1983)
Modified Horvath-Kawazoe	2001	Microporous	Slit	(Dombrowski et al. 2001)
Saito-Foley	1991	Microporous	Cylinder	(Saito and Foley 1991)

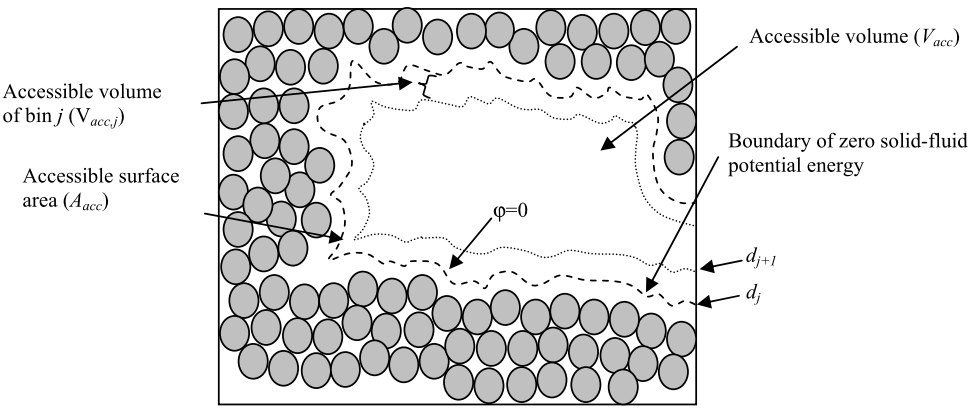

Fig. 1 Schematic diagram of the accessible volume and accessible surface area. The *dashed line* represents the boundary at which the solid-fluid potential energy is zero. The volume bounded by this boundary is the accessible volume. The space between the *dashed* and *dotted lines* is the accessible volume of bin j

insert a probe molecule at a random position in the simulation box enclosing a representative portion of the porous solid under consideration, and determine its potential energy with all solid atoms; this energy is calculated by summing all pairwise potential energies, and then we remove this probe particle from the box. If the solid-fluid potential is either zero or negative, that insertion is a success, otherwise is a failure. This insertion process is repeated many times to ensure that all the positions in the simulation box have an equal probability to be chosen. Finally, the accessible volume is the volume of the simulation box times the fraction of successful insertions (f):

$$V_{acc} = f\,V_{box}. \tag{1}$$

To calculate the accessible pore volume noble gases are preferred because they are inert, spherical and non-polar. Nitrogen is also a good candidate as it is the most widely used probe, but its adsorption may be specific (for example in zeolites carrying isolated cationic charges, or surfaces with high affinity functional groups) because its quadrupole favors strongly charged sites.

It is a common practice to calculate the gas phase volume from the simulation of helium expansion (Frost et al. 2006). It is known that helium adsorbs, especially in pores of molecular dimensions, and if its adsorption is neglected the gas phase volume is over estimated. This overestimation could compromise the determination of the Henry constant and isosteric heat (Do et al. 2008b, 2008c).

2.2 Geometrical accessible surface area

We define the surface area as the area of a boundary on which the solid-fluid potential energy is zero (see the dashed line in Fig. 1). To calculate this surface area, we extend the method presented in Sect. 2.1 for accessible pore volume one-step further. For each successful insertion, we determine the distance d, between the center of the successfully inserted particle and the center of the closest solid atom. If the distance d falls between the specified distances d_i and d_{i+1}, we store that successful insertion in the volume bin "i" (Fig. 1). After a large number of insertions have been carried out, the accessible volume of the bin "i" is the volume of the simulation box times the fraction of successful insertions that falls into that bin (f_i):

$$V_{acc,i} = f_i\,V_{box} \tag{2}$$

and the total accessible volume calculated by (1) can be also written as

$$V_{acc} = \sum_i V_{acc,i} \tag{3}$$

because $f = \sum_i f_i$.

Knowing the accessible volume of the bin "i" for all i, we compute the accessible area of the bin "i" as follows:

$$A_i = \frac{V_{acc,i}}{d_{i+1} - d_i}. \tag{4}$$

This can be regarded as the area at the distance $d_{i+1/2} = (d_i + d_{i+1})/2$ from the solid. At distances very close to the solid atoms the local accessible volume is zero (because of the repulsion by the solid atoms). The first non-zero A_i is defined as the interfacial solid-fluid area that satisfies the requirement of zero solid-fluid potential energy. We call this the *contact accessible surface area* or *solid-fluid interfacial surface area* (Do et al. 2010). In order to have a more accurate surface area, we calculate a set of different contact accessible surface areas $\{A_k\}$ by using different values of bin size, $\Delta = d_{k+1} - d_k$ (this can be done in the same process of obtaining the accessible volume). Once this is done we plot the first non-zero A_k as a function of Δ and the extrapolation of this to the zero axis (i.e. $\Delta \to 0$) gives the geometrical area of the boundary of the accessible volume.

This method was successfully applied by Herrera et al. (2010) to derive surface area of various solids such as defective slit pores, metal organic frameworks (MOF) and nanotube bundles. The use of this method is preferred to other methods, which are based on the pairwise interaction of a fluid particle and a solid atom (Gelb and Gubbins 1998; Thomson and Gubbins 2000; Frost et al. 2006). These methods fail in the derivation of the surface area for solids whose sizes are comparable to the size of the probe molecule (Herrera et al. 2010).

2.3 Pore size and pore volume

We have presented the methods to calculate the accessible volume and the accessible surface area based on the Monte Carlo integration. Let us now introduce the new concept of *accessible* pore size and develop a consistent method to determine the *accessible* pore size distribution.

To determine the pore size, we propose to use the diameter of a sphere as the yardstick and define the pore size as the size of a largest sphere which can be accommodated within the pore such that the solid-fluid potential energy of a probe particle, say argon, within this sphere is non-positive (Fig. 2) (Do et al. 2010). This pore size definition is *consistent* with the concepts of accessible volume and geometrical accessible surface area that we presented in Sects. 2.1 and 2.2, and we call this pore size the *accessible pore size*. From this definition of pore size, there is a pore size for every successful insertion in the pore. Therefore, the accessible pore size is a *local* variable, which reflects the different sizes in different parts of the pore. Figure 2 shows a 2D-representation of different pore sizes in the cavity of a typical porous structure.

Because there is a pore size for each non-positive potential point inside of the cavity of the pore, we start the determination of the *accessible* pore size distribution (A-PSD) with the location of one point in which the probe molecule has non-positive potential with the solid. Let A be the successful insertion point (Fig. 3) and our task is to determine the accessible pore size associated with it. First, we search for the three closest solid atoms on the solid surface from this insertion point A. Let these atoms be $S_1^{(\mathrm{I})}$, $S_1^{(\mathrm{II})}$ and $S_1^{(\mathrm{III})}$, with the first point being the closest to A and the last point being furthest from A. We present below an iterative procedure to search for the largest sphere such that the following two criteria are satisfied:

(1) this sphere encloses the insertion point A
(2) any point in this sphere has a non-positive solid-fluid potential.

We, hereafter, denote these criteria as ***C1*** and ***C2***. Since the desired largest sphere rests on three points on the solid surface, we shall coin this method the TriPOD method.

We proceed our iteration process by assigning the insertion point A and its associated three closest solid atoms as A_1, $S_1^{(\mathrm{I})}$, $S_1^{(\mathrm{II})}$ and $S_1^{(\mathrm{III})}$, with the subscript to denote the iteration number. We use the convention that the first point $S_1^{(\mathrm{I})}$ is the closest point to A_1 *on the surface* of the closest solid atom and the last point $S_1^{(\mathrm{III})}$ being the closest point to A_1

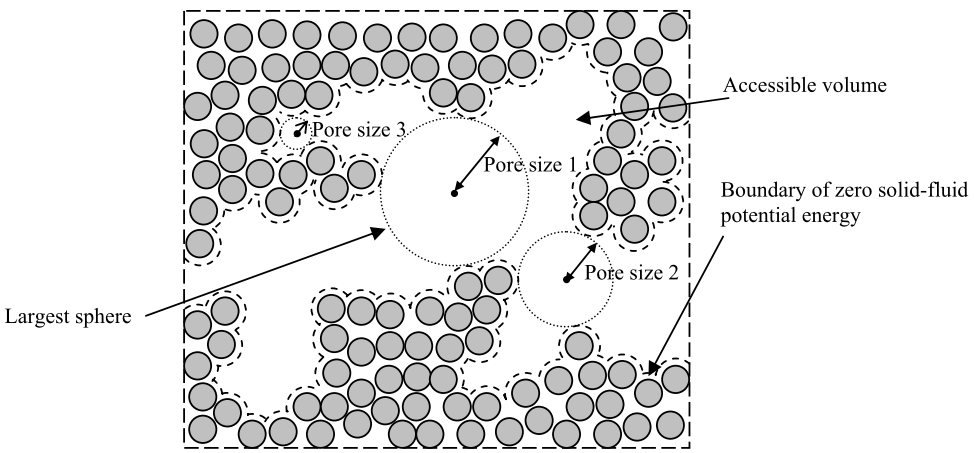

Fig. 2 Schematic diagram of the pore size. The *dashed line* represents the boundary at which the solid-fluid potential energy is zero. The volume bounded by this boundary is the accessible volume. The three different *pore size* inside of the same pore structure shows that the pore size is a local variable

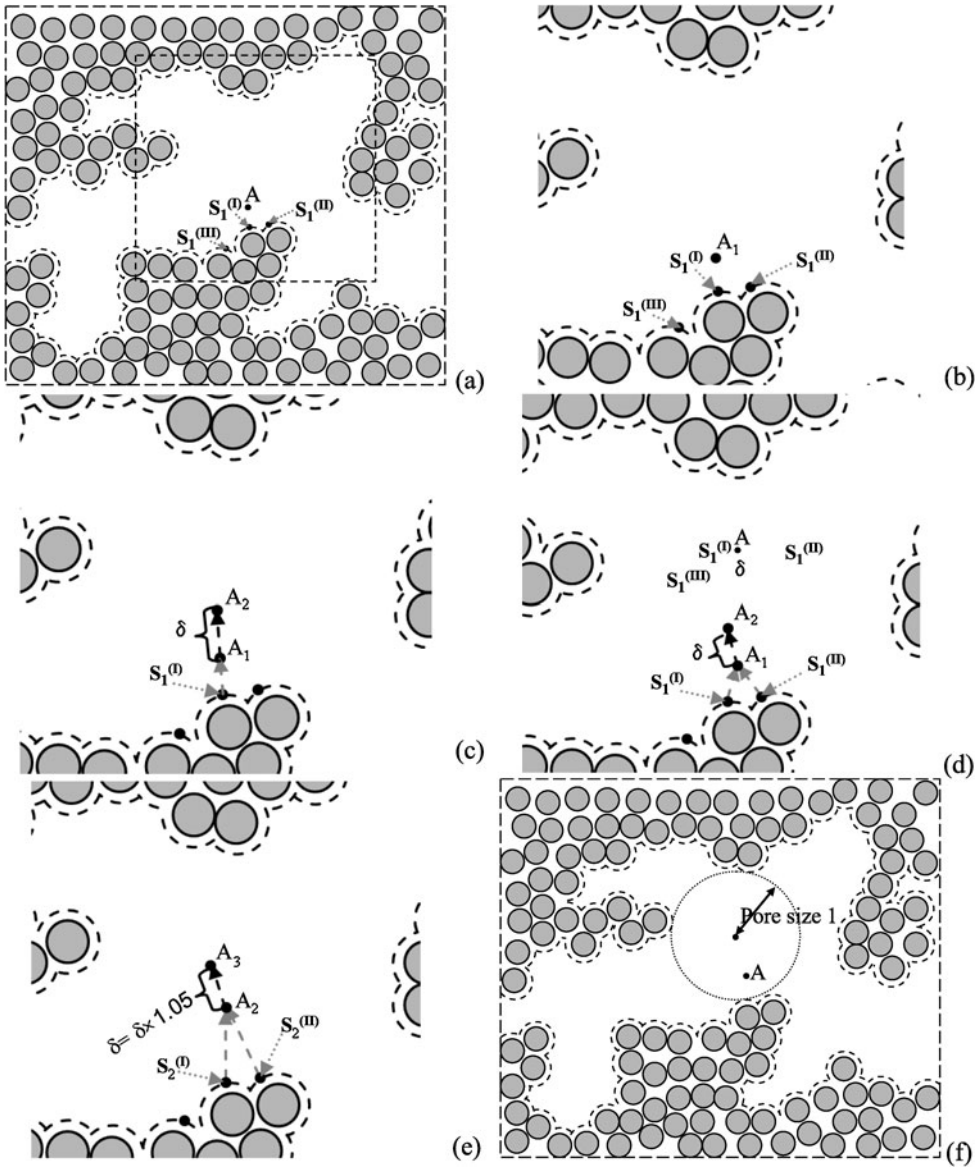

Fig. 3 Schematic diagram of the displacement of the center of the sphere according to the distance of the three closest solid atoms

on the surface of the third closest solid atom A_1 (Fig. 3a). This applies also to subsequent iterations. The algorithm is described below.

Algorithm:

1. Once A_1 has been chosen (i.e. a successful insertion point) and its three associated closest points on the solid surface are found, the next point in the iteration process depends on the distances $|A_1S_1^{(I)}|$, $|A_1S_1^{(II)}|$ and $|A_1S_1^{(III)}|$ (Figs. 3a and 3b). This completes the first iteration.
   a. If $|A_1S_1^{(I)}|$ is the shortest distance, we choose a new point A_2 along this vector $\overrightarrow{S_1^{(I)}A_1}$ by an increment δ (see Fig. 3c). We shall denote the initial increment as δ_0.
   b. If $|A_1S_1^{(I)}|$ and $|A_1S_1^{(II)}|$ are equal, then we move along the combined vector $\overrightarrow{S_1^{(I)}A_1} + \overrightarrow{S_1^{(II)}A_1}$ (Fig. 3d) to a new point A_2. In the case that the combined vector is zero, that is when the two solid atoms $S_1^{(I)}$ and $S_1^{(II)}$ are opposite to each other, we move along the vector $\overrightarrow{S_1^{(III)}A_1}$ by an increment δ to the new point A_2.
   c. If all the three distances $|A_1S_1^{(I)}|$, $|A_1S_1^{(II)}|$ and $|A_1S_1^{(III)}|$ are equal, we choose a new point A_2 along the vector $\overrightarrow{S_1^{(I)}A_1} + \overrightarrow{S_1^{(II)}A_1} + \overrightarrow{S_1^{(III)}A_1}$.
2. Once the position for A_2 has been estimated, we again find the three closest solid atoms on the surface, denoted them as $S_2^{(I)}$, $S_2^{(II)}$ and $S_2^{(III)}$. A sphere whose center at A_2 is constructed such that the criterion ***C2*** is met. There are two possibilities.

Table 2 Comparison between the original and the improved methods

Original method (Do et al. 2008a)	Proposed method	Correction
The determination of the three closest solid atoms is carried out sequentially.	The determination of the closest solid atoms is calculated simultaneously	The proposed method corrects the problems revealed in the previous method in deriving the correct pore size. The original method tends to underestimate it.
The distances of the three closest solid atoms are fixed during the entire path of the sphere to reach the final point.	The distances of the three closest solid atoms are recalculated every time the sphere is moved to a new position.	
The original method calculates the distances $\|A_n S_n^{(I)}\|$, $\|A_n S_n^{(II)}\|$ and $\|A_n S_n^{(III)}\|$ from the point A_n and the center of the solid atoms $S_n^{(I)}$, $S_n^{(II)}$ and $S_n^{(III)}$.	The distances $\|A_n S_n^{(I)}\|$, $\|A_n S_n^{(II)}\|$ and $\|A_n S_n^{(III)}\|$ are the distances between A_n and the points $S_n^{(I)}$, $S_n^{(II)}$ and $S_n^{(III)}$ on the surface of zero potential of the three closest solid atoms.	This modification allows calculating the A-PSD for solids made of solid atoms of different sizes.
The displacement of the sphere, δ, is constant along the path traced by the sphere.	The displacement of the sphere δ is varied during its displacement.	The incremental variation of δ during the derivation of the A-PSD helps to speed up the calculation.

   a. If the criterion ***C1*** is met, the position A_2 is accepted and we increase the displacement length δ by a factor of 1.05 for the next iteration ($\delta_1 = 1.05 \times \delta_0$). This completes the second iteration (Fig. 3e).
   b. If the criterion ***C1*** is not satisfied, what that means is that the sphere has reach its largest size because the closest solid atoms are closer to the center of the sphere than δ_0. Then the process is stopped because the pore size is less than δ_0. since δ_0 is so small the pore size is zero.
3. Once the position A_2 has been defined, the point A_3 is estimated as it was presented in step 1. Once again we fix A_3. base on two possibilities.
   a. If the criterion ***C1*** is met, the position A_3 is accepted and the displacement length δ is increased by a factor of 1.05 for the next iteration ($\delta_2 = 1.05 \times \delta_1$). This completes the third iteration.
   b. If the criterion $C1$ is not satisfied, we reset the increment δ to the initial value δ_0 to find the new position for A_3 until ***C1*** is fulfilled. Since the value of δ_0 is small enough of the order of $0.001 \times \sigma$ff, we consider that if ***C1*** cannot be satisfied with this value of δ_0, the largest size of the sphere has been reached and the iteration process is terminated, otherwise if ***C1*** is satisfied, we complete our third iteration.
4. We repeat the steps **1** to **3** until the distance travelled by the sphere between the current position A_n and the previous position A_{n-100}, $|A_n A_{n-100}|$ is below some acceptable threshold, for example δ_0 or any of the two criteria ***C1*** and ***C2*** is satisfied.
5. The size of the largest sphere in the whole iteration process is then taken to be the *accessible* pore size associated with the insertion point A (Fig. 3f).

The previous algorithm describes the method used to determine the accessible pore size for a specific insertion point A. To calculate the A-PSD, this method is repeated with many insertions at random positions in the simulation box. If the successful insertion has an accessible pore size D that falls between the specified pore sizes D_i and D_{i+1}. We store that successful insertion in the pore size bin i. After M insertions, the success fraction of pore size D falling between D_i and D_{i+1} is g_i then the accessible volume for that pore size is given by

$$V_{acc,i}\,(D_{i+1} < D < D_i) = g_i\, V_{box} \tag{5}$$

and the total accessible volume is $V_{acc} = \sum_j V_{acc,j}$.

The method presented in this paper removes problems associated with the previous method (Do et al. 2008a). The Table 2 shows the distinction between the two methods.

The minimum limit for the pore size and the pore volume The pore density is defined as the ratio of the number of moles adsorbed divided by the accessible volume ($\langle N \rangle / V_{acc}$). Since the definition of pore size is based on the accessible volume, and the minimum accessible pore size is zero, it is important to establish the value of the pore density at zero volume. Do and co-workers have demonstrated that the pore density in this limit of zero accessible volume is zero (Do et al. 2008a). This is because in these small pores (whose size is of the order of the probe molecule size) the adsorption amount decreases to zero faster than the accessible volume (Fig. 4) due to the strong repulsion close to the pore walls.

3 Results and discussion

We have presented a clear and unambiguous method to calculate the A-PSD based on the Monte Carlo (MC) integration. This method corrects the errors showed by the previous method (Do et al. 2008a) and we shall illustrate this with a number of model solids such as slit pore, defective slit pore,

carbon nanotubes and metal organic frameworks (MOFs). To derive the A-PSD we use noble gases as the probe molecules. The interaction potential between the probe molecule and the solid is calculated by using the Lennard Jones (LJ) potential model and the fluid-fluid LJ parameters for each noble gas are shown in Table 3.

Table 3 Fluid-fluid Lennard Jones parameters for the noble gases (Do and Do 2005, 2007)

Noble gas	Collision diameter (σ nm)	Well depth (ε/k_B K)
Helium	0.2556	10.22
Neon	0.2780	34.90
Argon	0.3405	119.80
Krypton	0.3685	164.40
Xenon	0.4047	231.00

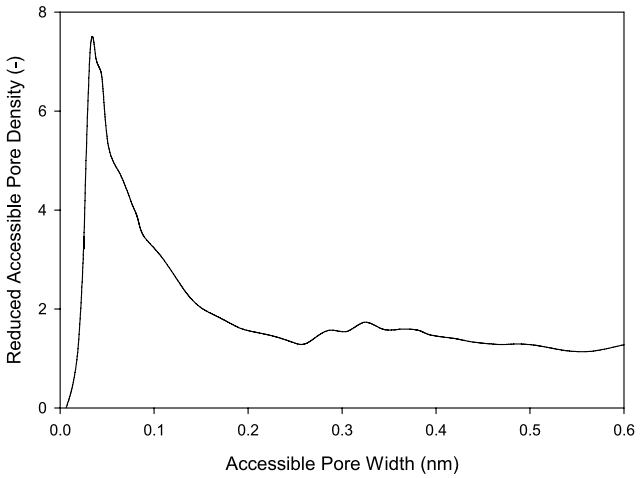

Fig. 4 Accessible pore density versus accessible pore width for argon adsorption in graphitic slit pores at 87.3 K (Do et al. 2008a)

3.1 Slit pore

We first apply the new method to a graphitic slit pore (Kaneko et al. 1998), whose accessible pore width can be estimated analytically. The two walls of the slit pore are composed of carbon atoms having a collision diameter of 0.34 nm, and the distance between two adjacent carbon atoms is 0.142 nm. We choose a pore having a physical width of 0.852 nm. The physical pore width is defined as the distance between the plane passing through carbon atoms of one wall to the corresponding plane of the opposite wall (Fig. 6).

If the pore is assumed to be homogeneous, we can readily calculate the accessible pore size H_{acc} from the 10-4-3 Steele potential. A pore volume distribution around this H_{acc} is anticipated from the Monte Carlo integration because of the corrugation of the surface. The closer the separation between the solid atoms, the smaller the corrugation and therefore the pore volume distribution will be much narrower. Figure 6 shows the A-PSD calculated from the previous method and the present modified one with argon used as a probe. Both methods calculate the accessible pore size of the slit pore to be around 0.28 nm, however the two methods display different features in the A-PSD. The previous method shows that for small pores (pore size less than 0.26 nm) the fraction of the accessible volume increases with the pore size, and then a rapid increase of the pore volume up to 30% of the total pore volume, for a pore size of 0.28 nm. The same plot shows the A-PSD derived with the improved method of this paper. This A-PSD shows a significantly less volume associated with small pores and a larger pore volume associated with the 0.28 nm pore size (41% of the total accessible volume). This difference in the A-PSD stems from the fact that the previous method (Do et al. 2008a) fails to determine the largest sphere. This is because it keeps the same solid atoms ($S_1^{(I)}$, $S_1^{(II)}$ and $S_1^{(III)}$) during the entire process to determine the largest sphere. The new method

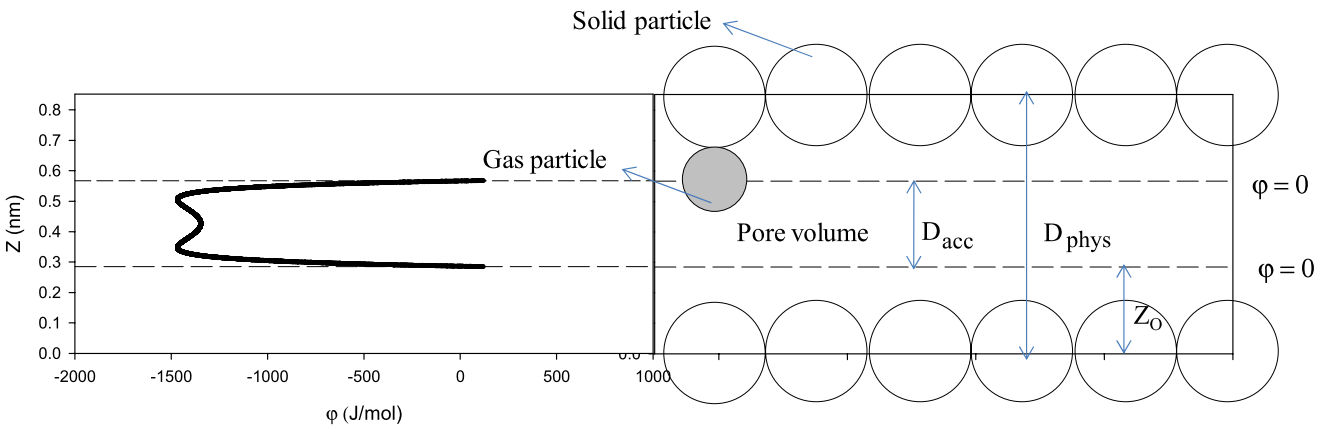

Fig. 5 Schematic diagram of the perfect slit pore of physical width H

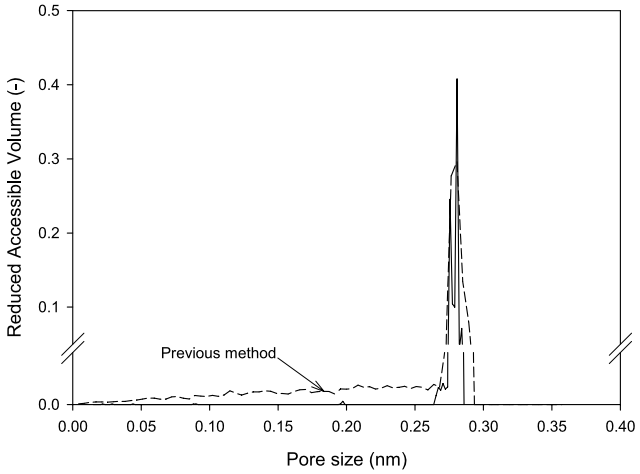

Fig. 6 Comparison between the A-PSD obtained from the initial and the improved method for a slit pore having physical width of 0.852 nm, when argon is used as a probe particle

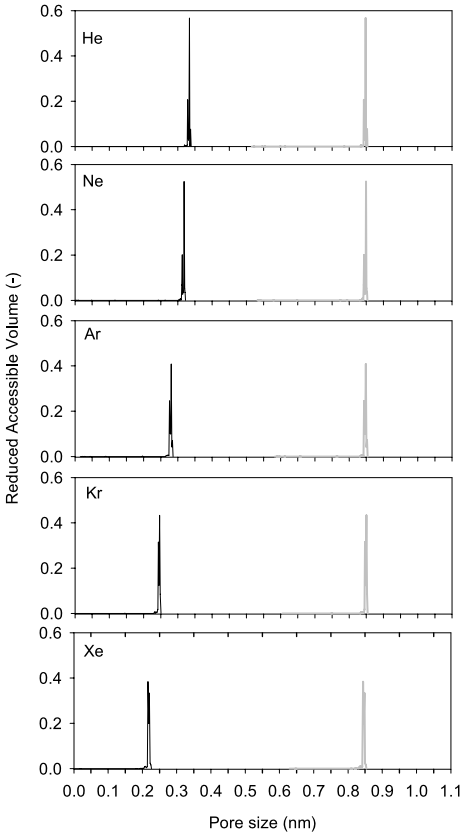

Fig. 7 Accessible pore volume plot versus accessible pore size for slit pores having physical width of 0.852 nm

corrects this by searching for the new three closest solid atoms every time that the sphere moves to a new position. This allows us the search for the proper largest sphere that can accommodate the insertion point.

Figure 7 shows the A-PSD calculated from different probe particles. The figure clearly demonstrates the importance of the role of adsorbate size in the determination of the accessible pore size distribution (A-PSD). This is expected because the A-PSD (or any PSDs for that matter) should be a function of the probe, and a smaller probe gives a larger accessible pore size because it can approach closer to the solid surface. Once the accessible pore size has been determined, the physical pore size can be obtained $D_{phys} = D_{acc} + 2 \times Z_0$, where Z_0 is the distance from the plane passing through the centers of solid atoms to the surface of zero solid-fluid potential (Fig. 5).

The physical pore size distributions, calculated for the slit pore by using all the noble gases, are also shown in Fig. 7 as gray plots. As expected, the physical pore size distributions for all noble gases are aligned at the physical pore width of 0.852 nm.

3.2 Defective pore

The next example is a defective graphitic pore. This pore is constructed by starting with a graphitic slit pore with two graphite layers in each wall. The two inner most layers are then modified to create defects. This can be done, for example, by methods suggested by Seaton et al. (1997), Turner and Quirke (1998), and Do et al. (2006). We follow the latter to construct a defective surface. In this method, the defects are created by selecting a carbon atom at random, and then it is removed together with its neighboring carbon atoms that fall within a specified radius from the selected atom. This

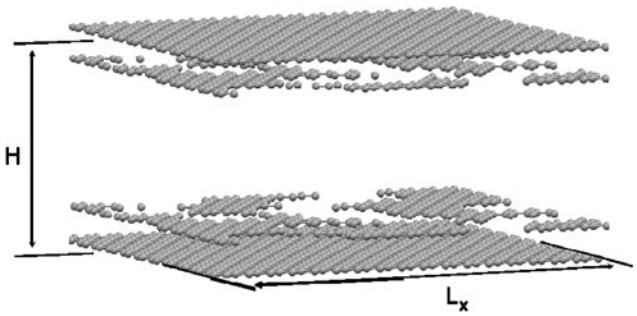

Fig. 8 Atomistic configuration of a defective pore

process is repeated to achieve the desired defect percentage. We calculate the A-PSD for a defective graphitic pore whose defect radius is 0.492 nm and the percentage of defect is 50%. Figure 8 shows this defective pore with H and L_x ($L_y = L_x$) equal to 2.2 and 4.6 nm, respectively.

The difference between the previous A-PSD method (Do et al. 2008a) and the improved one is more evident for this type of pore. This is shown in Fig. 9 when argon is used as the probe particle.

The accessible pore volume calculated with the previous method (Fig. 9a) shows a broad distribution of pore sizes below 1.0 nm, and then it peaks around a pore size of 0.97 nm.

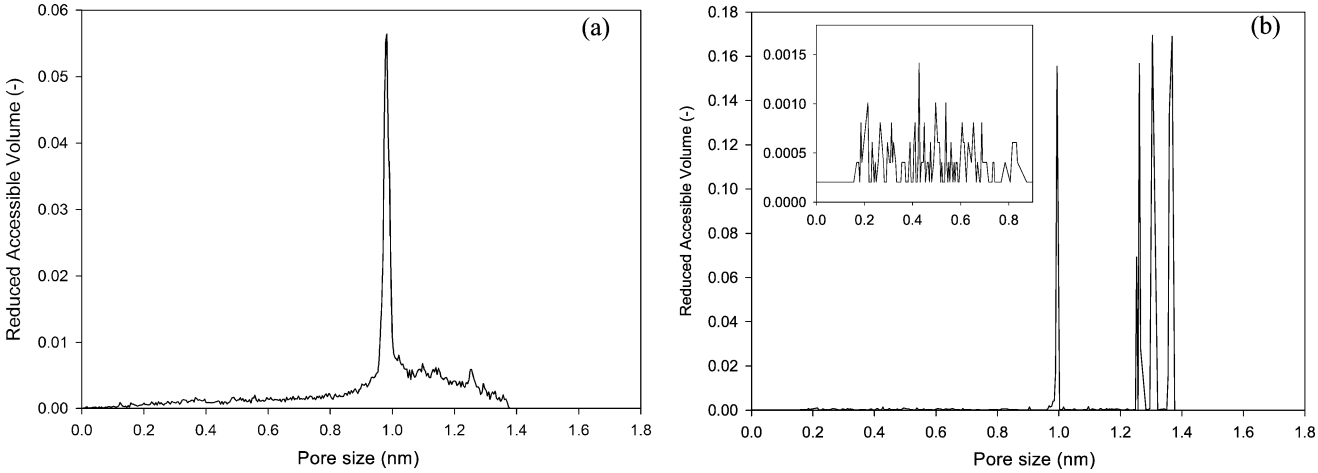

Fig. 9 Accessible pore volume plot versus accessible pore size for a defective slit pore. The figure (**a**) and (**b**) shows the results from the initial and improved A-PSD methods when argon is used as a probe particle

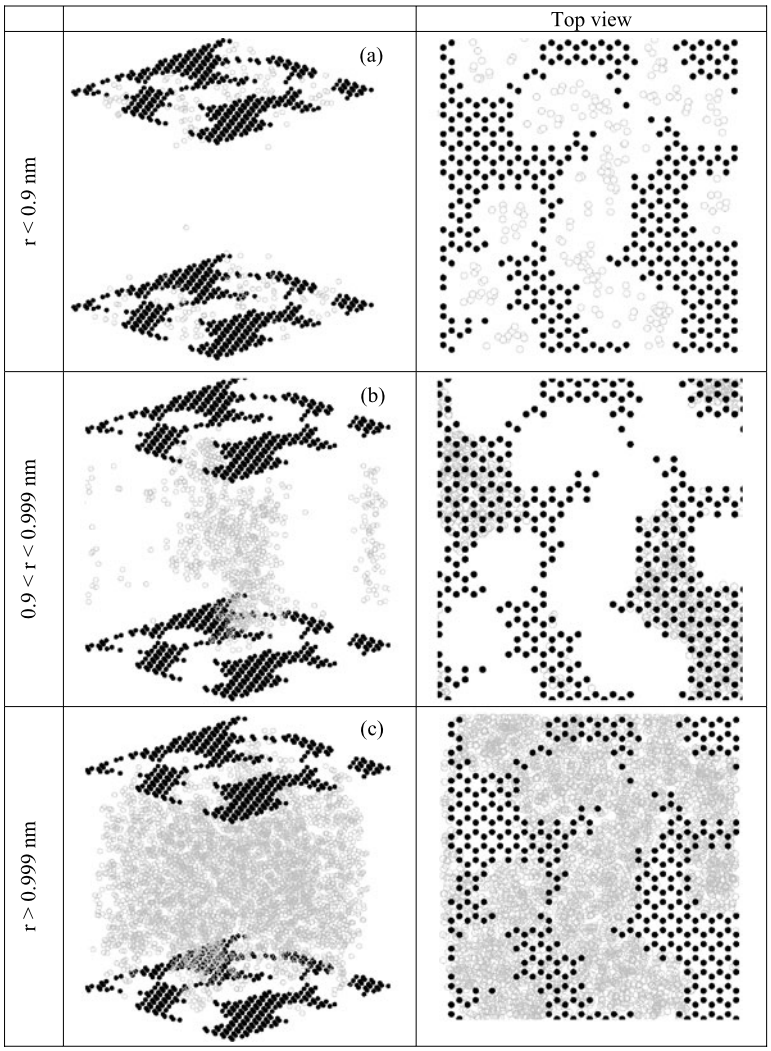

Fig. 10 Insertion points of the argon particles associated with the peaks in the accessible volume distribution of the defective pore. Figures (**a**), (**b**) and (**c**) show the insertion points for pores size $r < 0.9$, $0.9 < r < 0.999$ and $r > 0.999$ nm, respectively

This pore size is contributed by the volume space confined by the inner defected graphite layers. The maximum pore size is 1.38 nm, and this is attributed to the space between the outer graphite layers, through the defect holes of the inner layers. The original method (Do et al. 2008a) gives a zero pore volume associated with this maximum pore size, which is incorrect.

Figure 9b shows the A-PSD derived by using the improved method. It shows that the accessible volume associated to small pores within the defects in the two inner layers is less than 0.15% of the total accessible volume (some of the insertion points that fall in this volume is shown in Fig. 10a). Then we observe a sudden increase in the accessible volume up to 0.16 of the fraction of the total volume for a pore size of 0.97 nm. This peak is due to the pore volume between the two innermost graphene layers (Fig. 10b) and it agrees with the A-PSD shown in Fig. 9a. Then the A-PSD shows three consecutive peaks for pore sizes between 1.2 and 1.4 nm. These result from the spaces between the outer graphene layers (the accessible volume corresponding to these pores is shown in Fig. 10c). The effects of the probe size are shown in Fig. 11.

3.3 Metal organic framework

We compare the two A-PSD methods for the metal organic framework MOF-5, and derive the A-PSD for the MOF-10 and MOF-16 by using only the improved method. These MOF structures are porous cubic crystals formed by the connection between Zn_4O and benzene-1,4-dicarboxylate. The main difference between these MOFs is the ligand lengths, which are 0.5483, 0.9532 and 1.3581 nm for MOF-5, MOF-10 and MOF-16, respectively. The three MOF structures are shown in Fig. 12 (Civalleri et al. 2006; Walton and Snurr 2007). The LJ parameters for the solid atom in the MOF configurations are taken from Walton and Snurr (2007) and they are shown in Appendix.

The accessible pore size distributions derived from the previous method and the present one are shown in Fig. 13. These A-PSDs are derived by using argon as a probe molecule. The previous method shows a large accessible volume for pores sizes around 0.5 nm and a maximum pore size of 1.23 nm (Fig. 13a). The improved method shows that there are mainly two pore sizes of 0.87 and 1.23 nm (Fig. 13b). These results show that the pores around 0.5 nm obtained from the original method are due to the miscalculation of the largest sphere that fits within the pore, while the two

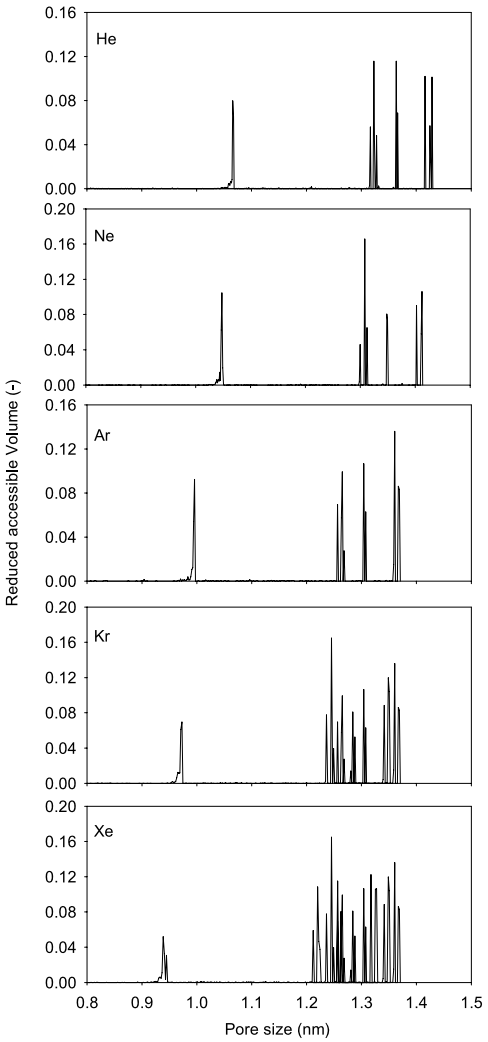

Fig. 11 A-PSDs derived from the noble gases for a defective slit pore

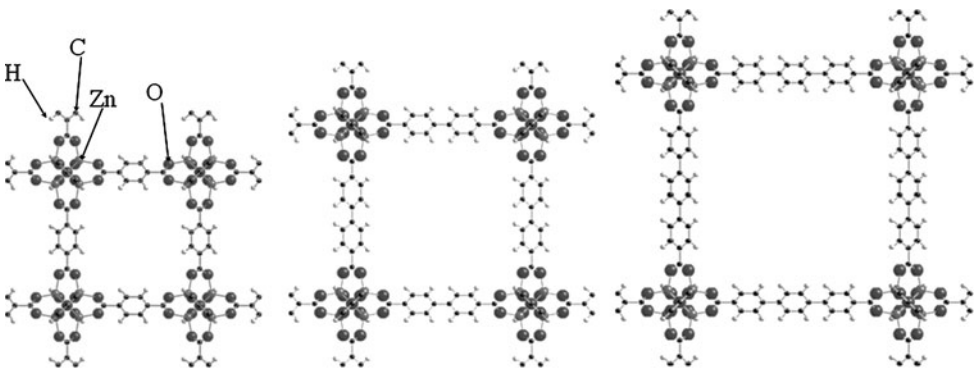

Fig. 12 Structures of MOF 5, MOF 10 and MOF 16, the solid atoms hydrogen, carbon, oxygen and zinc are indicated

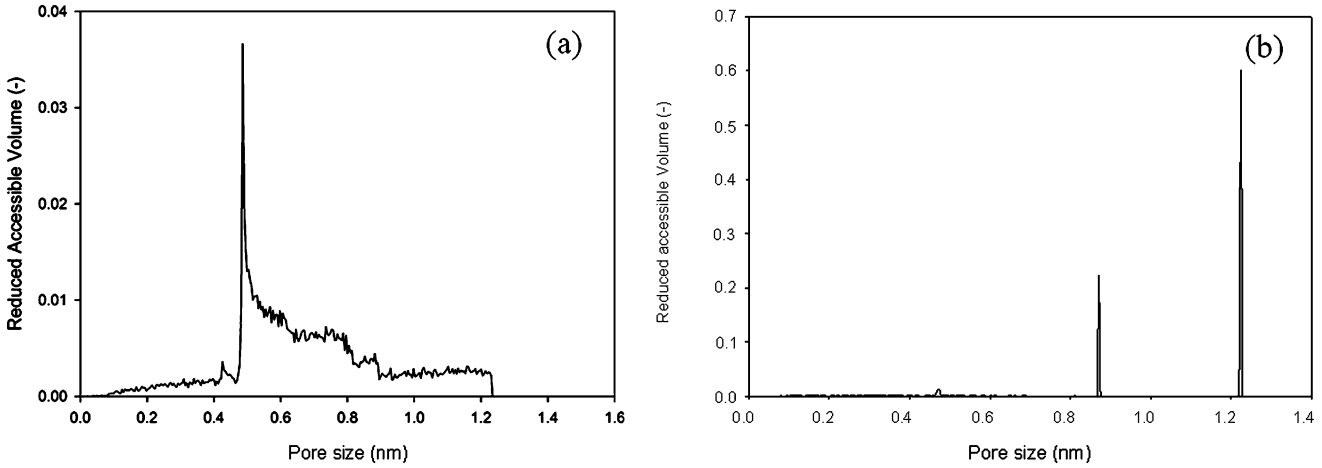

Fig. 13 Comparison of the accessible pore volume plot versus accessible pore size derived from the previous method (**a**) and the improved A-PSD method (**b**) by using argon for MOF-5

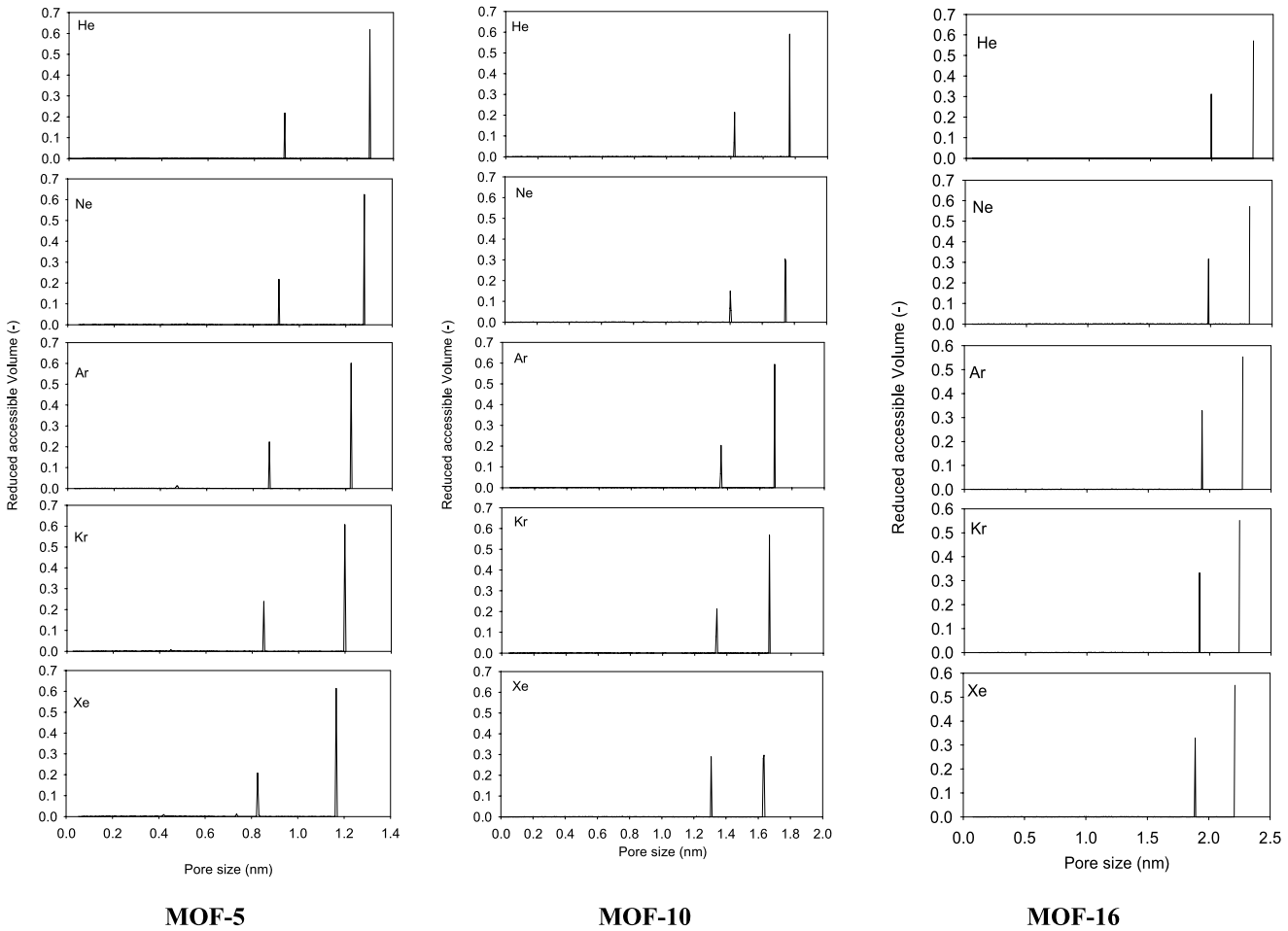

Fig. 14 Accessible pore volume plot versus accessible pore size derived from the noble gases for MOF-5, MOF-10 and MOF-16

methods agree in the size of the largest pore size. The physical pore size corresponding to the 0.87 and 1.23 nm accessible pore sizes are 1.182 and 1.542. This is because the main atom on the MOFs surface is the hydrogen and the combined collision diameter between argon and hydrogen is 0.3125 nm. The derived physical pore sizes agree with the

experimental results for 1.1 and 1.5 nm obtained with TEM image analysis by Turner et al. (2008).

Figure 14 shows the A-PSDs for MOF-5, MOF-10 and MOF-16 by using different probe particles. The results are consistent with other porous structures dealt with earlier, regarding the effect of probe size.

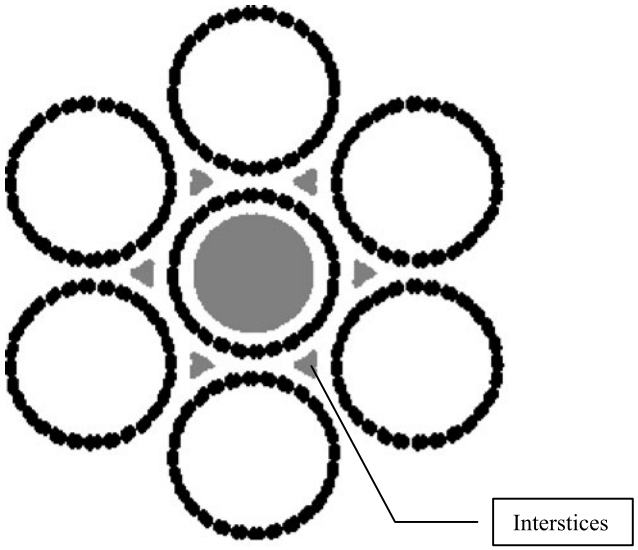

Fig. 15 Tube bundle of carbon nanotubes in a triangle configuration. The gray regions show the accessible volume in the inside and outside of the nanotube when helium is used as probe molecule

3.4 Tube bundle

Our next example is the bundle of carbon nanotubes. The carbon nanotubes are simulated by using carbon solid atoms. The distance between carbon atoms is 0.142 nm and the LJ carbon-carbon parameters, collision diameter and well depth of interaction energy are 0.34 nm and 28 K, respectively. The nanotubes are arranged in a hexagonal bundle around a central tube as shown in Fig. 15 and the physical radius of the nanotubes is 0.9451 nm.

In Fig. 16a we present the A-PSD of the nanotube bundle which includes the internal void space (inside the nanotube) and the interstices between the tubes, while in Fig. 16b we show the A-PSD the interstices only. It is interesting to see that the A-PSD for the interstices varies considerably with the probe size. For example, when helium is used there are two main pore sizes around 0.15 nm, in contrast xenon shows only one large peak at the pore size of 0.048 nm. This is because of the roughness of the interstices surface. The helium particle is smaller and can resolve better the irregularity of the surface due to the atomistic model used in the nanotubes than the xenon particle.

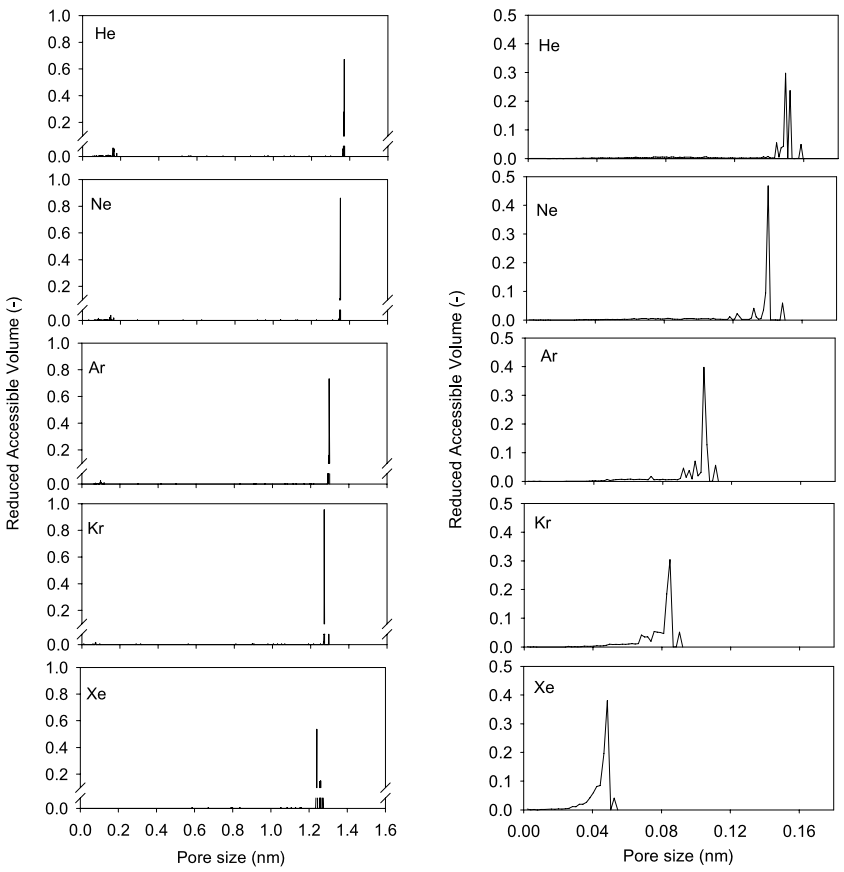

Fig. 16 Accessible pore volume plot versus accessible pore size derived from the noble gases for a nanotube bundle. The LHS and RHS show the A-PSD for the entire bundle and the interstices between nanotubes, respectively

3.5 Zeolite

Our last example is zeolite Li-ABW (Szostak 1992; Reed and Breck 1956) whose structure is shown in Fig. 17. The zeolite is a type A zeolite with pores of 0.34 × 0.38 nm. Its orthorhombic structure has $Pna2_1$ symmetry, and the unit cell $a = 1.0313$, $b = 0.8194$ and $c = 0.4993$ nm with the angles $\alpha = \beta = \gamma = 90$. The atomic coordinates of each atom are given in Table 4.

The accessible pore size distributions obtained from the previous method and from the improved one, using argon as a probe particle, are presented in Figs. 14a and 14b, respectively. The comparison between the two A-PSDs shows that the accessible volume is overestimated for small pores when the original method is used. The A-PSD derived from the improved method, on the other hand, shows a high peak around 14% of the total accessible volume for a pore size of 0.07 nm. Because the size of the probe molecule, argon, is about 0.305 nm, we have a physical pore size of 0.375 nm. This result agrees with the physical pore width of 0.38 nm (Szostak 1992).

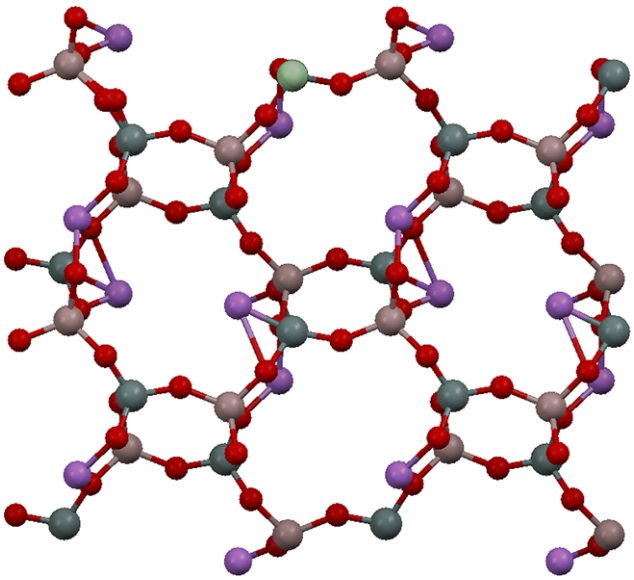

Fig. 17 Atomistic configuration of zeolite Li-ABW

4 Conclusions

We have presented an improved version of the Monte Carlo integration method to obtain the accessible pore volume as a function of accessible pore size for porous solids of known solid atom configuration. The previous method (Do et al. 2008a) fails to take account of the largest sphere that can be accommodated in the pore space. We have presented a corrected version of this method in this paper and have documented its application with several different pore structures. This accessible pore size distribu-

Table 4 Atomic coordinates for Li-ABW (Demontis et al. 2005) (nm)

	x/a ($\times 10^4$)	y/b ($\times 10^4$)	z/c ($\times 10^4$)
Li	1862	6849	2520
Al	1593	810	2500
Si	3544	3757	2492
O1	65	1584	1970
O2	2736	2198	1391
O3	1912	399	5907
O4	1804	−1008	689
O5	5891	903	−2395

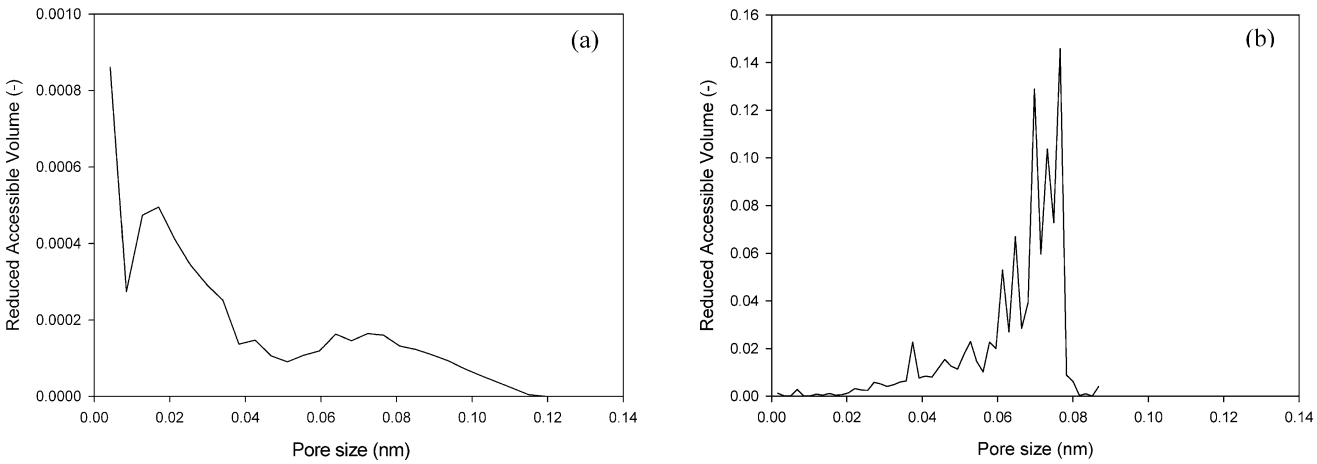

Fig. 18 Accessible pore volume plot versus accessible pore size for zeolite Li-ABW. The figure (**a**) and (**b**) show the results from the initial and the improved A-PSD methods when argon is used as a probe particle, respectively

tion is defined in an unambiguous manner and is in agreement with the accessible pore volume and the geometrical surface area obtained in our previous publications (Do and Do 2007; Do et al. 2010). The accessible pore volume, accessible geometrical surface area and the A-PSD offer a single and robust framework for the characterization of porous solids whose configuration is known. The potential of this method has been demonstrated with a number of porous solids, ranging from simple solids to complex ones.

Acknowledgement This work is supported by the Australian Research Council.

Appendix

Table A.1 The solid-solid Lennard Jones parameters for the solid atoms in MOF-5, MOF-10 and MOF-16 (Walton and Snurr 2007)

Noble gas	Collision diameter (σ nm)	Well depth (ε/k_B K)
Carbon	0.3472	47.886
Oxygen	0.3032	48.187
Hydrogen	0.2846	7.654
Zinc	0.4044	27.703

References

Barrett, E.P., Joyner, L.G., Halenda, P.P.: The determination of pore volume and area distribution in porous substances. I. Computations from nitrogen isotherms. J. Am. Chem. Soc. **73**, 373–380 (1951)

Broekhoff, J.C.P., De Boer, J.H.: Pore systems in catalysts. XII. Pore distributions from the desorption branch of a nitrogen sorption isotherm in the case of cylindrical pores. 1. An analysis of the capillary evaporation process. J. Catal. **10**(4), 368–376 (1968)

Civalleri, B., et al.: Ab-initio prediction of materials properties with crystal: MOF-5 as a case of study. CrystEngComm **8**, 364–371 (2006)

Demontis, P., Stara, G., Suffritti, G.B.: Molecular dynamics simulation of anomalous diffusion of one-dimensional water molecule chains in Li-ABW zeolite. Microporous Mesoporous Mater. **86**(1–3), 166–175 (2005)

Do, D.D., Do, H.D.: Effects of potential models in the vapor–liquid equilibria and adsorption of simple gases on graphitized thermal carbon black. Fluid Phase Equilibria **236**(1–2), 169–177 (2005)

Do, D.D., Do, H.D.: Modeling of adsorption on nongraphitized carbon surface: GCMC simulation studies and comparison with experimental data. J. Phys. Chem. B **110**(35), 17531–17538 (2006)

Do, D.D., Do, H.D.: Appropriate volumes for adsorption isotherm studies: The absolute void volume, accessible pore volume and enclosing particle volume. J. Colloid Interface Sci. **316**(2), 317–330 (2007)

Do, D.D., Herrera, L.F., Do, H.D.: A new method to determine pore size and its volume distribution of porous solids having known atomistic configuration. J. Colloid Interface Sci. **328**, 110–119 (2008a)

Do, D.D., Nicholson, D., Do, H.D.: On the Henry constant and isosteric heat at zero loading in gas phase adsorption. J. Colloid Interface Sci. **324**(1–2), 15–24 (2008b)

Do, D.D., et al.: Henry constant and isosteric heat at zero-loading for gas adsorption in carbon nanotubes. Phys. Chem. Chem. Phys. **10**, 7293–7303 (2008c)

Do, D.D., Herrera, L.F., Do, H.D., Nicholson, D.: A method for the determination of accessible surface area, pore volume, pore size and its volume distribution for homogeneous pores of different shapes. Adsorption J. (2010, in press)

Dombrowski, R.J., Lastoskie, C.M., Hyduke, D.R.: The Horvath-Kawazoe method revisited. Colloids Surf. A, Physicochem. Eng. Asp. **187**, 23–39 (2001)

Dubinin, M.M., Stoeckli, H.F.: Homogeneous and heterogeneous micropore structures in carbonaceous adsorbents. J. Colloid Interface Sci. **75**(1), 34–42 (1980)

Frost, H., Düren, T., Snurr, R.Q.: Effects of surface area, free volume, and heat of adsorption on hydrogen uptake in metal-organic frameworks. J. Phys. Chem. B **110**(19), 9565–9570 (2006)

Gelb, L.D., Gubbins, K.E.: Characterization of porous glasses: simulation models, adsorption isotherms, and the Brunauer-Emmett-Teller analysis method. Langmuir **14**, 2097–2111 (1998)

Gregg, S.J., Sing, K.S.W.: Adsorption, Surface Area and Porosity, A. Press (ed.), p. xi, 303. Academic Press, San Diego (1982)

Herrera, L., Do, D.D., Nicholson, D.: A Monte Carlo integration method to determine accessible volume, accessible surface area and its fractal dimension. J. Colloid Interface Sci. **348**(2), 529–36 (2010)

Horvath, G., Kawazoe, K.: Method for the calculation of effective pore size distribution in molecular sieve carbon. J. Chem. Eng. Jpn. **16**(6), 470–475 (1983)

Kaneko, K., et al.: Characterization of porous carbons with high resolution α-analysis and low temperature magnetic susceptibility. Adv. Colloid Interface Sci. **76–77**, 295–320 (1998)

Kaneko, K., et al.: Role of gas adsorption in nanopore characterization. In: Studies in Surface Science and Catalysis, pp. 11–18. Elsevier, Amsterdam (2002)

Li, H., et al.: Design and synthesis of an exceptionally stable and highly porous metal-organic framework. Nature **402**, 476–479 (1999)

Reed, T.B., Breck, D.W.: Crystalline zeolites. II. Crystal structures of synthetic zeolite, type A. J. Am. Chem. Soc. **78**, 5972–5977 (1956)

Rouquerol, F., Rouquerol, J., Sing, K.: Adsorption by Powders and Porous Solids Principles, Methodology and Applications, A. Press (ed.), p. 465. Academic Press, New York (1999)

Rouquerol, J., et al.: Recommendations for the characterization of porous solids. Pure Appl. Chem. **66**(8), 1739–1758 (1994)

Rowsell, J.L.C., Yaghi, O.M.: Metal–organic frameworks: a new class of porous materials. Microporous Mesoporous Mater. **73**, 3–14 (2004)

Saito, A., Foley, H.C.: Curvature and parametric sensitivity in models for adsorption in micropores. AIChE **37**(3), 429–436 (1991)

Seaton, N.A., et al.: The molecular sieving mechanism in carbon molecular sieves: a molecular dynamics and critical path analysis. Langmuir **13**(5), 1199–1204 (1997)

Sing, K.S.W., et al.: Reporting physisorption data for gas/solid systems with special reference to the determination of surface area and porosity (recommendations 1984). Pure Appl. Chem. **57**(4), 603–619 (1985)

Szostak, R.: Handbook of Molecular Sieves, p. 584. Van Nostrand Reinhold, New York (1992)

Thomson, K.T., Gubbins, K.: Modeling structural morphology of microporous carbons by reverse Monte Carlo. Langmuir **16**(13), 5761–5773 (2000)

Turner, A.R., Quirke, N.: A grand canonical Monte Carlo study of adsorption on graphitic surfaces with defects. Carbon **36**(10), 1439–1446 (1998)

Turner, S., et al.: Direct imaging of loaded metal-organic framework materials (metal@MOF-5). Chem. Mater. **20**(17), 5622–5627 (2008)

Walton, K.S., Snurr, R.Q.: Applicability of the BET method for determining surface areas of microporous metal-organic frameworks. J. Am. Chem. Soc. **129**, 8552–8556 (2007)